Molecules with ALMA at Planet-forming Scales (MAPS): A Circumplanetary Disk Candidate in Molecular-line Emission in the AS 209 Disk

Jaehan Bae[1] , Richard Teague[2,3] , Sean M. Andrews[2] , Myriam Benisty[4,5] , Stefano Facchini[6] ,
Maria Galloway-Sprietsma[1] , Ryan A. Loomis[7] , Yuri Aikawa[8] , Felipe Alarcón[9] , Edwin Bergin[9] ,
Jennifer B. Bergner[10,27] , Alice S. Booth[11] , Gianni Cataldi[8,12] , L. Ilsedore Cleeves[13] , Ian Czekala[14,15,16,17] ,
Viviana V. Guzmán[18] , Jane Huang[9,27] , John D. Ilee[19] , Nicolas T. Kurtovic[20] , Charles J. Law[2] , Romane Le Gal[21,22] ,
Yao Liu[23] , Feng Long[2] , François Ménard[4] , Karin I. Öberg[2] , Laura M. Pérez[24,25] , Chunhua Qi[2] ,
Kamber R. Schwarz[20] , Anibal Sierra[24] , Catherine Walsh[19] , David J. Wilner[2] , and Ke Zhang[26]

[1] Department of Astronomy, University of Florida, Gainesville, FL 32611, USA; jbae@ufl.edu
[2] Center for Astrophysics | Harvard & Smithsonian, 60 Garden Street, Cambridge, MA 02138, USA
[3] Department of Earth, Atmospheric, and Planetary Sciences, Massachusetts Institute of Technology, Cambridge, MA 02139, USA
[4] Univ. Grenoble Alpes, CNRS, IPAG, F-38000 Grenoble, France
[5] Université Côte d'Azur, Observatoire de la Côte d'Azur, CNRS, Laboratoire Lagrange, France
[6] Universitá degli Studi di Milano, via Celoria 16, I-20133 Milano, Italy
[7] National Radio Astronomy Observatory, 520 Edgemont Road, Charlottesville, VA 22903, USA
[8] Department of Astronomy, Graduate School of Science, The University of Tokyo, Tokyo 113-0033, Japan
[9] Department of Astronomy, University of Michigan, 323 West Hall, 1085 S. University Avenue, Ann Arbor, MI 48109, USA
[10] University of Chicago, Department of the Geophysical Sciences, Chicago, IL 60637, USA
[11] Leiden Observatory, Leiden University, 2300 RA Leiden, The Netherlands
[12] National Astronomical Observatory of Japan, 2-21-1 Osawa, Mitaka, Tokyo 181-8588, Japan
[13] Department of Astronomy, University of Virginia, Charlottesville, VA 22904, USA
[14] Department of Astronomy and Astrophysics, 525 Davey Laboratory, The Pennsylvania State University, University Park, PA 16802, USA
[15] Center for Exoplanets and Habitable Worlds, 525 Davey Laboratory, The Pennsylvania State University, University Park, PA 16802, USA
[16] Center for Astrostatistics, 525 Davey Laboratory, The Pennsylvania State University, University Park, PA 16802, USA
[17] Institute for Computational & Data Sciences, The Pennsylvania State University, University Park, PA 16802, USA
[18] Instituto de Astrofísica, Pontificia Universidad Católica de Chile, Av. Vicuña Mackenna 4860, 7820436 Macul, Santiago, Chile
[19] School of Physics and Astronomy, University of Leeds, Leeds, LS2 9JT, UK
[20] Max-Planck-Institut für Astronomie, Königstuhl 17, D-69117, Heidelberg, Germany
[21] Institut de Planétologie et d'Astrophysique de Grenoble (IPAG), Université Grenoble Alpes, CNRS, F-38000 Grenoble, France
[22] Institut de Radioastronomie Millimétrique (IRAM), 300 rue de la piscine, F-38406 Saint-Martin d'Hères, France
[23] Purple Mountain Observatory & Key Laboratory for Radio Astronomy, Chinese Academy of Sciences, Nanjing 210023, People's Republic of China
[24] Departamento de Astronomía, Universidad de Chile, Camino El Observatorio 1515, Las Condes, Santiago, Chile
[25] Núcleo Milenio de Formación Planetaria (NPF), Chile
[26] Department of Astronomy, University of Wisconsin-Madison, 475 N Charter Street, Madison, WI 53706, USA

Abstract

We report the discovery of a circumplanetary disk (CPD) candidate embedded in the circumstellar disk of the T Tauri star AS 209 at a radial distance of about 200 au (on-sky separation of $1''4$ from the star at a position angle of 161°), isolated via ^{13}CO $J = 2-1$ emission. This is the first instance of CPD detection via gaseous emission capable of tracing the overall CPD mass. The CPD is spatially unresolved with a 117×82 mas beam and manifests as a point source in ^{13}CO, indicating that its diameter is $\lesssim 14$ au. The CPD is embedded within an annular gap in the circumstellar disk previously identified using ^{12}CO and near-infrared scattered-light observations and is associated with localized velocity perturbations in ^{12}CO. The coincidence of these features suggests that they have a common origin: an embedded giant planet. We use the ^{13}CO intensity to constrain the CPD gas temperature and mass. We find that the CPD temperature is $\gtrsim 35$ K, higher than the circumstellar disk temperature at the radial location of the CPD, 22 K, suggesting that heating sources localized to the CPD must be present. The CPD gas mass is $\gtrsim 0.095 M_{Jup} \simeq 30 M_{\oplus}$ adopting a standard ^{13}CO abundance. From the nondetection of millimeter continuum emission at the location of the CPD (3σ flux density $\lesssim 26.4 \mu Jy$), we infer that the CPD dust mass is $\lesssim 0.027 M_{\oplus} \simeq 2.2$ lunar masses, indicating a low dust-to-gas mass ratio of $\lesssim 9 \times 10^{-4}$. We discuss the formation mechanism of the CPD-hosting giant planet on a wide orbit in the framework of gravitational instability and pebble accretion.

[27] NASA Hubble Fellowship Program Sagan Fellow.

1. Introduction

One of the best and most direct ways to study planet formation processes is to observe young planets while they are forming. Although this task has long been challenging, the situation is rapidly changing. In particular, recent observations

with the Atacama Large Millimeter/submillimeter Array (ALMA) have demonstrated the possibility of detecting young planets by spatially and kinematically resolving the characteristic gas flows around forming planets (see review by Pinte et al. 2022), including localized velocity perturbations associated with planet-driven spirals (Pinte et al. 2018; Casassus & Pérez 2019) and large-scale meridional flows falling onto planet-hosting gaps (Teague et al. 2019a; Yu et al.2021).

As a giant planet forms, it opens a radial gap in its natal circumstellar disk (Lin & Papaloizou 1986). Within the Hill (or Bondi) sphere of the planet, a circumplanetary disk (CPD) forms in order to conserve the angular momentum of the material accreted from the circumstellar disk (Korycansky et al. 1991; Ward & Canup 2010). The growth of a planet after gap opening is controlled by gas accretion through its CPD (Lubow et al. 1999). CPDs also play a crucial role in satellite formation. Indeed, the prograde, nearly circular, and coplanar orbits of regular satellites of Jupiter and Saturn suggest that their formation must have happened within CPDs. Despite their importance, however, many attempts to search for CPDs have yielded nondetections (Isella et al. 2014; Pérez et al. 2019; Pineda et al. 2019; Andrews et al. 2021), and the detections made to date are limited in millimeter continuum observations (Isella et al. 2019; Benisty et al. 2021; Wu et al. 2022). Consequently, fundamental properties of CPDs, such as their sizes (see discussion in Paardekooper et al. 2022) and whether they are indeed rotationally supported "disks" or instead pressure-supported envelopes (Szulágyi et al. 2016; Fung et al. 2019) are not fully understood.

In this Letter, we report the discovery of a CPD candidate embedded in the circumstellar disk of AS 209, identified using ^{13}CO $J = 2 - 1$ emission. AS 209 is a T Tauri star located in the outskirts of the Ophiuchus star-forming region at a distance of 121 pc (Gaia Collaboration et al. 2021), with a stellar mass of $1.2\,M_\odot$ and an age of 12 Myr (Andrews et al. 2009; Öberg et al. 2021, and references therein). In (sub)millimeter continuum emission, the AS 209 disk is $\simeq 140$ au in size and has multiple pronounced concentric rings and gaps (Fedele et al. 2018; Guzmán et al. 2018; Huang et al. 2018; Sierra et al. 2021). Hydrodynamic planet–disk interaction simulations showed that the continuum gaps can be explained by one or more planets embedded in the disk (Fedele et al. 2018; Zhang et al. 2018). The gas disk probed by ^{12}CO emission extends to $\simeq 300$ au, much farther out than the continuum disk (Guzmán et al. 2018). In ^{12}CO, an annular gap is seen centered at a radius of 200 au, sandwiched by two bright rings whose intensities peak at 168 and 245 au (Guzmán et al. 2018; Law et al. 2021a). Near-infrared scattered-light observations also revealed this gap around 200 au (Avenhaus et al. 2018). This ^{12}CO and near-infrared gap at 200 au is within which the CPD candidate is found in this study.

This Letter is organized as follows. In Section 2, we summarize the observations. In Section 3, we present the ^{12}CO data, which reveal an annular gap and localized kinematic perturbations, and the ^{13}CO data, which show a CPD candidate. We also present a null detection of $C^{18}O$ and continuum emission at the location of the CPD candidate. In Section 4, we place constraints on the size, temperature, and mass of the CPD and discuss the potential formation pathway of the planet. We summarize our findings and state our conclusions in Section 5.

2. Observations

The ^{12}CO, ^{13}CO, and $C^{18}O$ data used in this study were obtained as part of the ALMA Large Program Molecules with ALMA at Planet-forming Scales (MAPS; 2018.1.01055.L; Öberg et al. 2021). We refer the reader to Öberg et al. (2021) for the observational setup and calibration process and to Czekala et al. (2021) for the imaging process including the Jorsater & van Moorsel (1995, hereafter JvM) correction, which is used to properly scale the CLEAN residual map into consistent units of Janskys per CLEAN beam (instead of Janskys per dirty beam) and is crucial for correctly estimating the flux density of faint extended emission. Throughout this paper, we use the `robust=0.5` weighted, JvM-corrected images[28] unless stated otherwise. The ^{12}CO, ^{13}CO, and $C^{18}O$ images have synthesized beam sizes of 134×100 mas, 140×104 mas, and 141×105 mas with position angles of $-89°.2$, $-89°.1$, and $-88°.6$, respectively. The rms noise measured in line-free channels is 0.605 mJy beam^{-1}, 0.447 mJy beam^{-1}, and 0.337 mJy beam^{-1}, respectively.

While the JvM correction allows the CLEAN model and residual image to have consistent units, Casassus & Carcamo (2022) cautioned that it may exaggerate the peak signal-to-noise ratio of restored images. As such, we carry out our analyses using both JvM-corrected images (presented in the main sections) and JvM-uncorrected images (presented in Appendix C) in order to ensure that the CPD detection is statistically significant regardless of which image we use.

For the analysis of continuum data, we combined the continuum data from ALMA Large Programs MAPS and Disk Substructures at High Angular Resolution Project[29] (DSHARP; 2016.1.00484.L; Andrews et al. 2018), using CASA version 6.4. We refer the reader to Sierra et al. (2021) for the imaging of the MAPS continuum data and to Andrews et al. (2018) for the observational setup and calibration process of the DSHARP continuum data. To account for any source proper motions or atmospheric/instrumental effects between observations, we aligned each data set to a common phase center using the `fixvis` and `fixplanets` tasks to apply the necessary phase shifts. We then made a composite image at 240 GHz, the mean frequency of the DSHARP and MAPS continuum data. The continuum image was generated with a Briggs weighting scheme with `robust=0.5` and a 65×20 mas FWHM Gaussian taper (at PA $= 0°$) in order to enhance the point-source sensitivity near the location of the CPD candidate. The synthesized beam has an FWHM of 106×94 mas at a position angle of $-69°.2$. We find that the PSF of the combined data is complex due to the combined u, v coverage of the data sets. For that reason, we do not perform the JvM correction on the continuum data. The rms noise within an elliptical annulus $\pm 0''.1$ around the radial location of the CPD candidate (i.e., between $1''.6$ and $1''.8$ in the deprojected plane) is $8.8\,\mu$Jy beam^{-1}.

The DSHARP and MAPS observations were taken about two years apart. Between the two observations, the CPD candidate is expected to have moved about 8 mas in the sky, less than 10% of the synthesized beam of the combined
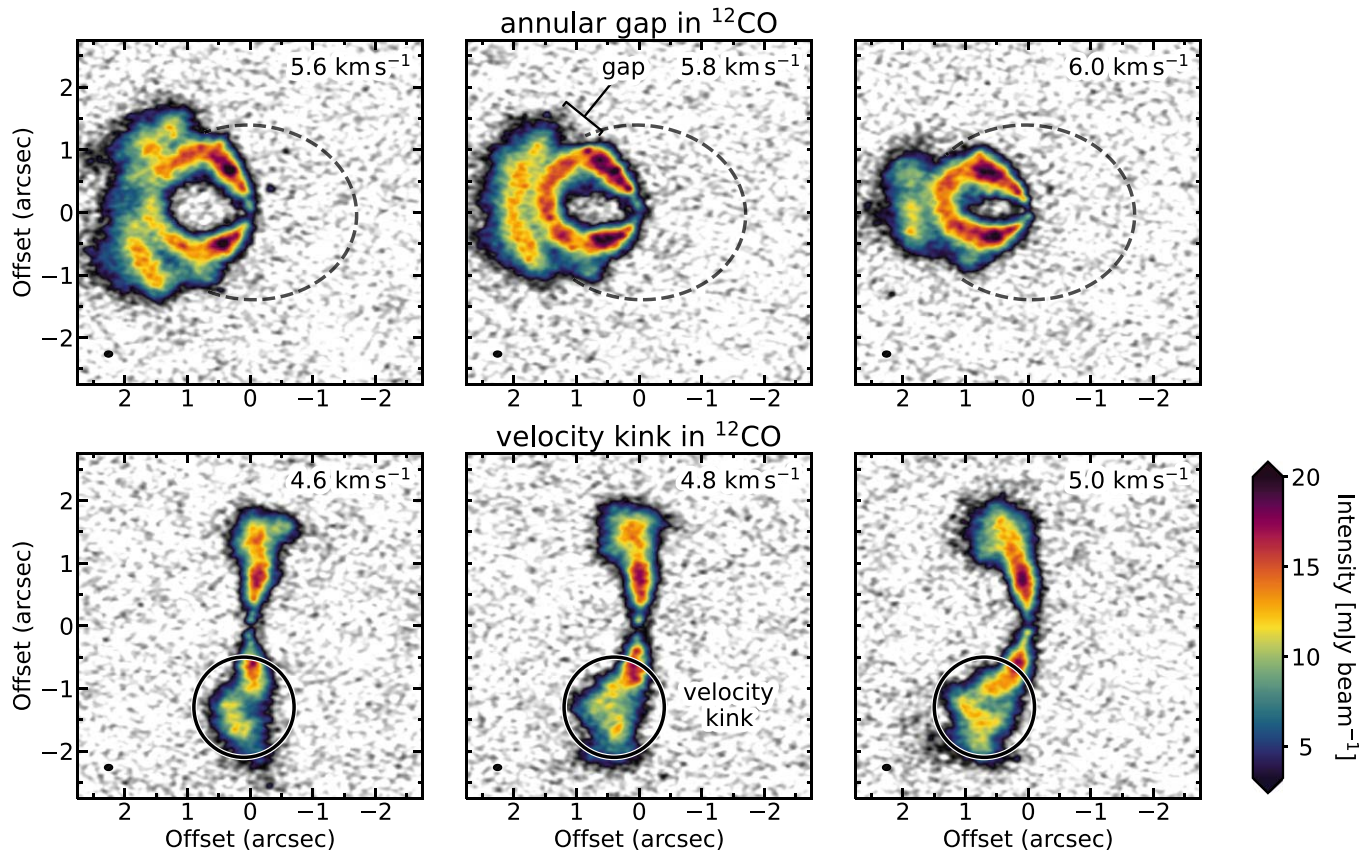

Figure 1. Selected ^{12}CO $J = 2-1$ channel maps. The upper panels show an annular gap. The black dashed ellipses present the projected circular orbit with a radius of 206 au. Lower panels show a large velocity perturbation on the southern side of the disk (highlighted with black circles). A similar perturbation is not present on the northern side of the disk, emphasizing the localized nature of the perturbation. The synthesized beam is presented in the lower-left corner of each panel. The color map starts at $5\sigma \simeq 3.3$ mJy beam^{-1}.

continuum data. We thus opt not to account for the orbital motion of the CPD candidate.

3. Results

3.1. An Annular Gap and Localized Kinematic Perturbations in ^{12}CO

We present selected ^{12}CO channel maps in Figure 1 (see Figure 7 in Appendix A for additional channel maps). The ^{12}CO emission reveals a 78 au-wide gap (determined by the distance between the adjacent peaks in the radial intensity profile; Law et al. 2021a) around $\simeq$200 au, which is most clearly seen along the semimajor axis of the disk (see 5.6–6.0 km s^{-1} in Figure 1). The radial location of the gap is consistent with what is previously reported in Guzmán et al. (2018) and Teague et al. (2018) using independent ^{12}CO data sets, and in Avenhaus et al. (2018) using near-infrared scattered-light images. Teague et al. (2018) showed that the ^{12}CO gap is associated with deviations in the rotational motion of the gas with variations of up to 5% relative to the background Keplerian rotation, which arises from the steep radial gas pressure gradient at the edges of the gap. While we defer more comprehensive kinematic studies to a forthcoming paper (M. Galloway-Sprietsma et al. 2022, in preparation), comparable rotational velocity deviations are found around the ^{12}CO gap using the MAPS ^{12}CO data.

In addition to the annular gap, ^{12}CO reveals a strong localized (both in space and velocity) perturbation on the southern side (see 4.6–5.0 km s^{-1} in Figure 1), reminiscent of a so-called velocity kink induced by planets (Pinte et al. 2018).

Similar velocity perturbations are found at the same location and velocity in independent archival ^{12}CO data sets presented in Guzmán et al. (2018) and Teague et al. (2018). The velocity perturbation is seen near the semiminor axis of the disk, suggesting that the perturbation is associated with radial and/or vertical motions rather than rotational motions (Teague et al. 2019b). We note that a similar velocity perturbation is not seen on the northern side of the disk, highlighting the localized nature of the perturbation.

3.2. Point-Source Emission in ^{13}CO

Figure 2 presents selected ^{13}CO channel maps (see Figures 8 and 9 in Appendix A for additional channel maps). In addition to the characteristic butterfly pattern arising from the Keplerian rotation of the AS 209 disk, we find a point-source emission at a projected distance of 1″4 and a position angle of 161° (east from north). The offset from the star (assumed to be at the center of the concentric continuum rings) is (ΔR.A., Δdecl.) = (0″450 ± 0.004, −1″332 ± 0.003). Assuming that the point source is embedded in the midplane of the AS 209 disk, the deprojected distance between the point source and the central star is 1″7 ($\simeq$206 au). It is worth pointing out that the ^{13}CO point source is located at the center of the ^{12}CO annular gap and is coincident in both radius and azimuth with the localized velocity perturbations seen in ^{12}CO. In Section 4.1, we will discuss the potential (common) origin of these features.

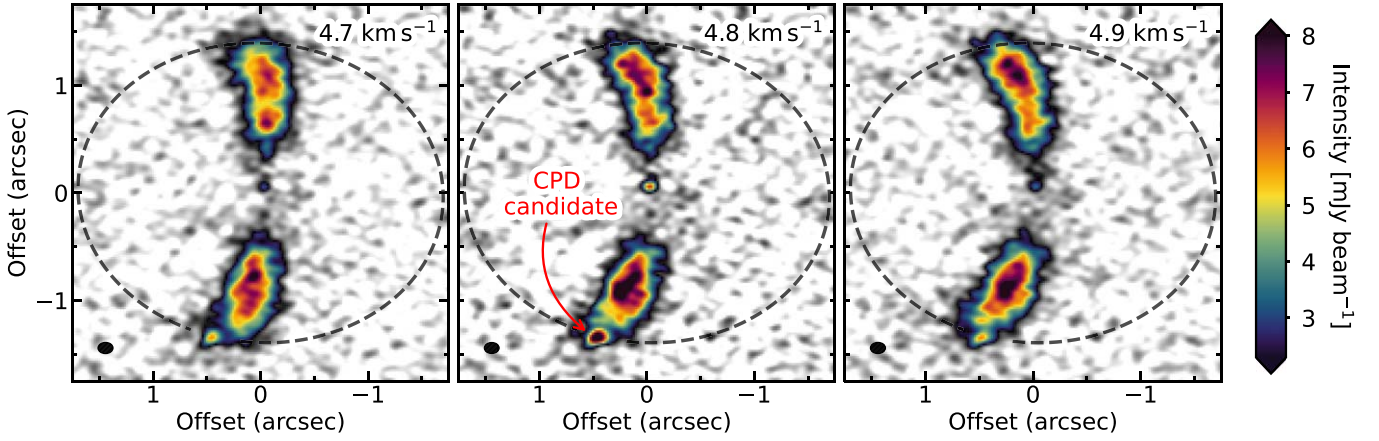The ^{13}CO data are limited by the 200 m s^{-1} velocity resolution set by the MAPS program. In the fiducial image

Figure 2. Selected ^{13}CO $J = 2-1$ channel maps. A point source is seen at a projected distance of $1''4$ with a position angle of $161°$ (east from north). The dashed ellipses show the projected circular orbit of an object with an orbital semimajor axis of 206 au. Near the center of the AS 209 disk, the inner disk appears as a point source because of an annular gap around $\simeq 0''5$ (Law et al. 2021a; see also Figure 3). The synthesized beam is presented in the lower-left corner of each panel. The color map starts at $5\sigma \simeq 2.3$ mJy beam^{-1}.

cube, the point source is found in two adjacent channels, 4.7 km s^{-1} (Figure 2, left) and 4.9 km s^{-1} (Figure 2, right). The peak intensities at the two channels are 5.75 and 5.85 mJy beam^{-1}, respectively. While we cannot image at a finer channel spacing than the velocity resolution, we produce an additional image cube with the same channel spacing of 200 m s^{-1}, but with the starting velocity offset by half of the velocity resolution (100 m s^{-1}). The middle panel in Figure 2 shows the channel map at 4.8 km s^{-1} from the half-channel-shifted image cube. The point source is more clearly seen, with the peak intensity of 9.62 mJy beam^{-1} (rms noise = 0.543 mJy beam^{-1}). Simply comparing the peak intensity with the rms noise, the point source in the three velocity channels is detected above the 12σ, 18σ, and 13σ levels, respectively.

Although the ^{13}CO emission from the AS 209 disk is less extended than the ^{12}CO emission, ^{13}CO emission is detected out to $\simeq 2''$ (in deprojected distance), beyond the radial location of the point source. If the point source is embedded in the midplane within the ^{12}CO gap, it is thus possible that some of the emission toward the point source originates from the residual gas within the gap. To assess the potential contamination from the gas in the gap, in Figure 3 we present a radial profile of the integrated intensity averaged over the azimuthal region $\pm 2°$ around the point source. We compare that to an azimuthally averaged, radial integrated intensity profile excluding the $\pm 2°$ region around the point source. At the deprojected radial distance of $1''7$, the integrated intensity of the point source is 2.54 mJy beam^{-1} km s^{-1}, while the integrated intensity excluding the point source is 1.15 mJy beam^{-1} km s^{-1} with a standard deviation of 0.33 mJy beam^{-1} km s^{-1}.

The brightness temperature of the ^{13}CO emission within the gap (excluding the point source) is $\lesssim 8$ K. For a reasonable gas temperature of $\gtrsim 20$ K (so that CO does not freeze), the gap must be optically thin ($\tau_{gap} \lesssim 0.5$) because the brightness temperature is lower than the gas temperature. The fact that the integrated intensity toward the point source does not increase with the beam size (see Appendix B) further supports that the gap is optically thin in ^{13}CO and the point source dominates the emission. If we assume that a similar amount of gas is present around the point source to elsewhere within the gap, the contamination from the gas in the gap is thus expected to be $1.15/2 = 0.575$ mJy beam^{-1} km s^{-1} (because only half of the gas in front of the point source would contribute). Subtracting this from the integrated intensity toward the point source, we find that the point source is detected at a 6.0σ
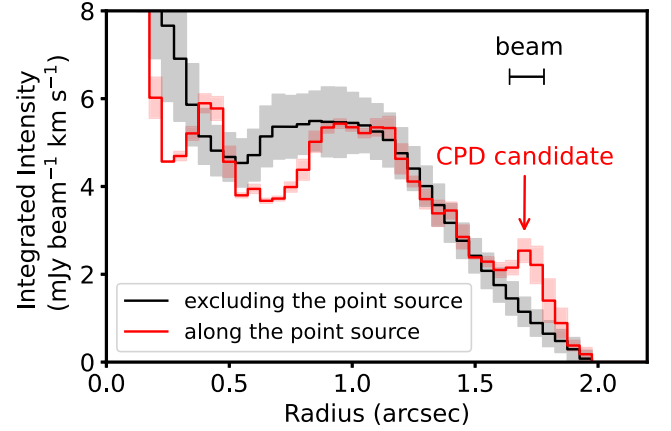

Figure 3. (Red) Radial profile of the ^{13}CO integrated intensity along the location of the point source, averaged over $\pm 2°$ in position angle around the point source. (Black) Azimuthally averaged radial profile of the ^{13}CO integrated intensity excluding the point source. The gray and red shaded regions show the standard deviation of the integrated intensity in each $0''05$ radial bin. The point source is seen well above the azimuthally averaged integrated intensity. The gap at $\simeq 0''5-0''6$ is consistent with the ^{13}CO gap previously reported by Law et al. (2021a). The size of the major axis of the synthesized beam is shown with the black horizontal bar.

significance. We carry out the same analysis using the JvM-uncorrected image and find that the point source is detected at a 4.4σ significance (see Appendix C).

In order to determine whether or not the point source is spatially resolved, we follow Isella et al. (2019) and Benisty et al. (2021) and image the data using various robust parameters ranging from -1 to 2. The synthesized beam size, rms noise, and Gaussian fit to the point-source emission are summarized in Appendix B. We find that the peak and integrated intensities are constant within uncertainties when the semiminor axis of the beam is $\lesssim 120$ mas, indicating that the point source is spatially unresolved at those scales. For larger beam sizes, the peak and integrated intensities increase because the point source is no longer spatially separated from the AS 209 disk.

3.3. Null Detection in C^{18}O and Continuum

In Figure 4, we present C^{18}O $J = 2-1$ emission at 4.8 km s^{-1} and the continuum image. No C^{18}O emission at a
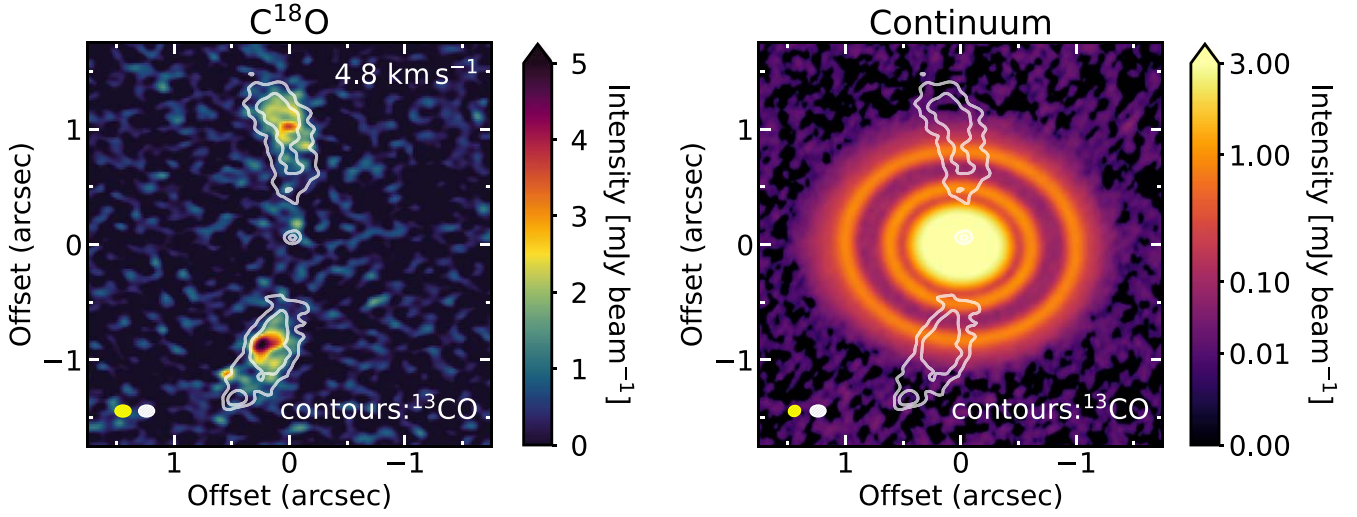
Figure 4. (Left) $C^{18}O$ $J = 2-1$ channel map at 4.8 km s^{-1}, which is the velocity that the ^{13}CO point source has the largest intensity. (Right) The combined MAPS + DSHARP continuum image. The color table is saturated toward the disk center and stretched to better show faint emission at large radii. In both panels, the white contours show the ^{13}CO $J = 2-1$ emission at 4.8 km s^{-1} at 5σ and 10σ levels. In the lower-left corner of each panel, synthesized beams for the $C^{18}O$ and continuum data are shown with yellow ellipses while the synthesized beam for the ^{13}CO data is shown with white ellipses.

$>3\sigma$ significance is detected at the location of the ^{13}CO point source. Similarly, no emission coincident with the ^{13}CO point source is detected at a $>3\sigma$ significance in the continuum image. We further inspected the continuum data by modeling the continuum emission in the visibility plane following Andrews et al. (2021), but no point-source emission coincident with the ^{13}CO point source (and elsewhere) is found. In Section 4.2, we place upper limits on the CPD gas and dust masses based on the null detection of $C^{18}O$ and continuum emission.

4. Discussion

4.1. Origin of the ^{13}CO Point Source

We find that the ^{13}CO point source lies at the center of the ^{12}CO gap and that it is colocated with the ^{12}CO velocity kink (Figure 5). The coincidence suggests that the most likely explanation is that we are witnessing a planet and its CPD embedded in the AS 209 disk. In fact, the compact nature of the ^{13}CO emission separated from the circumstellar disk bears a striking resemblance to what is predicted in numerical simulations of a CPD embedded in a circumstellar disk presented in Perez et al. (2015). There is no obvious counterpart to the ^{13}CO point source in ^{12}CO, but this is likely because the annular gap is optically thick in ^{12}CO. Similarly, we do not find a counterpart to the ^{12}CO velocity kink in ^{13}CO or $C^{18}O$ due to their low optical depth within and beyond the circumstellar disk gap (see, e.g., Figure 5(d)).

Recent numerical simulations have shown that circumplanetary materials form a rotationally supported disk when the cooling is efficient, but when cooling is inefficient, a pressure-supported envelope is instead formed (Szulágyi et al. 2016; Fung et al. 2019). The point source is spectrally unresolved in the existing data set, and whether the emission is associated with a disk or an envelope has to be confirmed in the future using high-velocity-resolution molecular-line observations that can probe the kinematics of the point source. For the rest of this paper, we opt not to distinguish between the CPD and envelope, but simply use the term CPD to refer to the two collectively.

What is the mass of the planet candidate? We can estimate the planet mass using the empirical relation between the gap width and planet mass derived from numerical simulations. The width of the gap, determined by the distance between the adjacent peaks in the ^{12}CO radial intensity profile, is 78 au (Law et al. 2021a). The scaling relation between the gap width normalized by the planet's orbital semimajor axis $\Delta_{\mathrm{gap}}/R_p$, disk aspect ratio $(h/r)_p$, disk viscosity α, and planet mass M_p suggests $\Delta_{\mathrm{gap}}/R_p = 0.41(M_p/M_*)^{0.5}(h/r)_p^{-0.75}\alpha^{-0.25}$ (Kanagawa et al. 2016; see also similar relations in, e.g., Zhang et al. 2018; Yun et al. 2019). Adopting the disk aspect ratio at the midplane $(h/r)_p = 0.118$ from the circumstellar disk temperature constrained using CO isotopologues (Law et al. 2021b), $\Delta_{\mathrm{gap}}/R_p = 0.38$ converts to a planet mass of $M_p = 1.3\,M_{\mathrm{Jup}} \cdot (\alpha/10^{-3})^{1/2}$. The inferred mass is comparable to those suggested to explain velocity kinks in other circumstellar disks (e.g., Pinte et al. 2018, 2019).

4.2. Properties of the CPD

4.2.1. CPD Size and Temperature

As shown in Appendix B, the CPD is spatially unresolved. When the CPD is optically thick and the disk gas is in local thermodynamic equilibrium (LTE), the actual CPD gas temperature, T_{CPD} (assumed to be uniform across the CPD for simplicity), and the observed brightness temperature of the CPD, T_{obs}, are related as $T_{\mathrm{obs}} = \epsilon T_{\mathrm{CPD}}$ where ϵ is the beam dilution factor.[30] Adopting a thin-disk geometry, the beam dilution factor is given by

$$\epsilon = \frac{f\,D_{\mathrm{CPD}}^2\cos i}{\theta_{\mathrm{maj}}\theta_{\mathrm{min}}/\ln 2}, \quad (1)$$

where f is a dimensionless parameter introduced to account for the fraction of the emitting area in a given velocity channel compared to the full geometric area of the CPD (see below),

---

[30] Here, we assume that the gap is optically thin in ^{13}CO (see Section 3.2) and ignore attenuation of the CPD emission by the residual gas in the circumstellar disk gap. The inferred CPD temperature thus offers a lower limit on the actual CPD temperature.
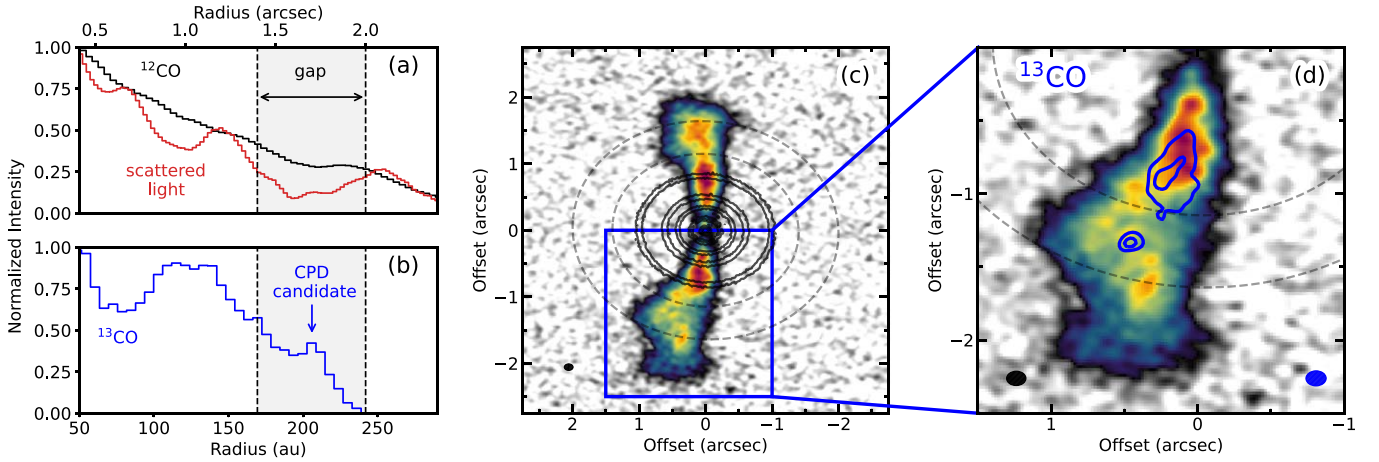
Figure 5. A summary figure showing the coincidence of the CPD candidate with the ^{12}CO/scattered-light gap and ^{12}CO velocity kink. (a) Radial profiles of the normalized (black) ^{12}CO integrated intensity and (red) the near-infrared scattered light (from Avenhaus et al. 2018; scaled by r^2 to account for the drop in the incident stellar photons). The shaded region shows $1\farcs4$–$2\farcs0$, the approximate radial location of the ^{12}CO gap. (b) Radial profile of the normalized ^{13}CO integrated intensity along the azimuthal location of the CPD (see Figure 3). (c) ^{12}CO channel map at 4.8 km s^{-1}. The location of the ^{12}CO gap is shown with the gray dashed ellipses. Black contours show the dust continuum from Andrews et al. (2018). (d) A zoom-in of the blue box in panel (c), showing the velocity kink in ^{12}CO (background color map) within the ^{12}CO gap (black dashed curves). The blue contours show ^{13}CO emission at 10σ and 15σ levels. Note that the CPD candidate is located at the center of the ^{12}CO gap and coincides with the velocity kink in ^{12}CO, highly suggestive of the presence of an embedded planet. The synthesized beams for ^{12}CO and ^{13}CO data are shown in the lower-left and lower-right corners of the panel, respectively.

$D_{\rm CPD}$ is the diameter of the CPD, i is the inclination of the CPD, and $\theta_{\rm maj}$ and $\theta_{\rm min}$ are the semimajor and semiminor axis of the synthesized beam, respectively. We can then relate the temperature and diameter of the CPD as

$$T_{\rm CPD} = T_{\rm obs} \frac{\theta_{\rm maj}\theta_{\rm min}/\ln 2}{f\,D_{\rm CPD}^2 \cos i}. \tag{2}$$

Without the knowledge of the emitting area, we opt to adopt $f = 1$, although it is reasonable to expect $f < 1$ because the channel spacing of the data (200 m s^{-1}) is smaller than the FWHM of the line emission arising from the CPD (300–400 m s^{-1}; see Appendix B). With $f = 1$, our analysis thus offers a lower limit on the CPD temperature. We use the brightness temperature in the 4.8 km s^{-1} channel ($\simeq$19 K) because it is likely that the channel contains the largest emitting area. We adopt $i = 35°$ (Öberg et al. 2021) assuming that the CPD and AS 209's circumstellar disk are coplanar.

Figure 6(a) shows the CPD temperature required to explain the observed ^{13}CO emission as a function of the CPD diameter, calculated with Equation (2). We note again that the CPD temperature in Figure 6(a) presents a lower limit because a higher CPD temperature is needed to explain the observed ^{13}CO emission (1) when attenuation by the gas in the circumstellar disk gap is not negligible, (2) when the emitting area in the central channel is smaller than the full geometric area of the CPD ($f < 1$), and/or (3) when the CPD is optically thin. We find that the CPD temperature is $\gtrsim$35 K, higher than the circumstellar disk gas temperature at the radial location of the CPD, 22 K (Law et al. 2021b). This suggests that additional heating sources localized to the CPD are required to explain the observed ^{13}CO emission, such as the planet's thermal/accretion heating, the CPD's internal viscous/turbulent heating, or shock/compressional heating by infalling circumstellar disk material (Szulágyi et al. 2016; Szulágyi & Mordasini 2017).

In the discussion above (and also below in Section 4.2.2), we assume that the CPD and AS 209's circumstellar disk are coplanar. This is a reasonable assumption to start, but

numerical simulations show that it is possible that CPDs and their parent circumstellar disk can be misaligned if the planet is formed in a turbulent environment (Jennings & Chiang 2021). In fact, based on the observationally constrained large obliquity of a planetary-mass ($M_p = 12$–$27\,M_{\rm Jup}$) companion 2M0122b, 48^{+28}_{-21} deg, Bryan et al. (2020) proposed that the CPD of 2M0122b would have to be tilted out of the circumstellar disk plane (see also Bryan et al. 2021). For our analysis, the CPD temperature would be minimized when the CPD is face on ($i = 0°$; see Equation (2)). However, even when the CPD is face on, we infer the CPD temperature to be $\gtrsim$29 K, higher than the circumstellar disk temperature, suggesting that additional heating sources localized to the CPD are still required. Future high-spatial/velocity-resolution observations would constrain the CPD geometry from its rotation, allowing us to place more accurate constraints on the CPD temperature.

4.2.2. CPD Mass

For a given CPD size and the corresponding lower limit on the CPD temperature (black curve in Figure 6(a)), we can place a lower limit on the ^{13}CO mass. This is possible because the upper-state energy of the ^{13}CO $J = 2-1$ transition (15.8 K) is below the lower limit of the CPD temperature; the population in the $J = 2$ rotational level would always drop if the CPD temperature is higher than the lower limit, requiring a larger CPD mass than for cooler temperatures.

To obtain the total ^{13}CO number density in the CPD, we first calculate the number density of ^{13}CO molecules in the $J = 2$ level as

$$n_{^{13}{\rm CO},J=2} = \frac{4\pi}{hcA_{21}} \int I dv \int d^2 d\Omega, \tag{3}$$

where h is the Planck constant, $A_{21} = 6.04 \times 10^{-7}$ s^{-1} is the spontaneous emission coefficient from molecular data from the LAMDA database (Schöier et al. 2005), $\int I dv = 2.50$ mJy beam^{-1} km s^{-1} is the integrated line intensity, d is the distance to AS 209, 121 pc (Gaia Collaboration et al. 2021), and Ω
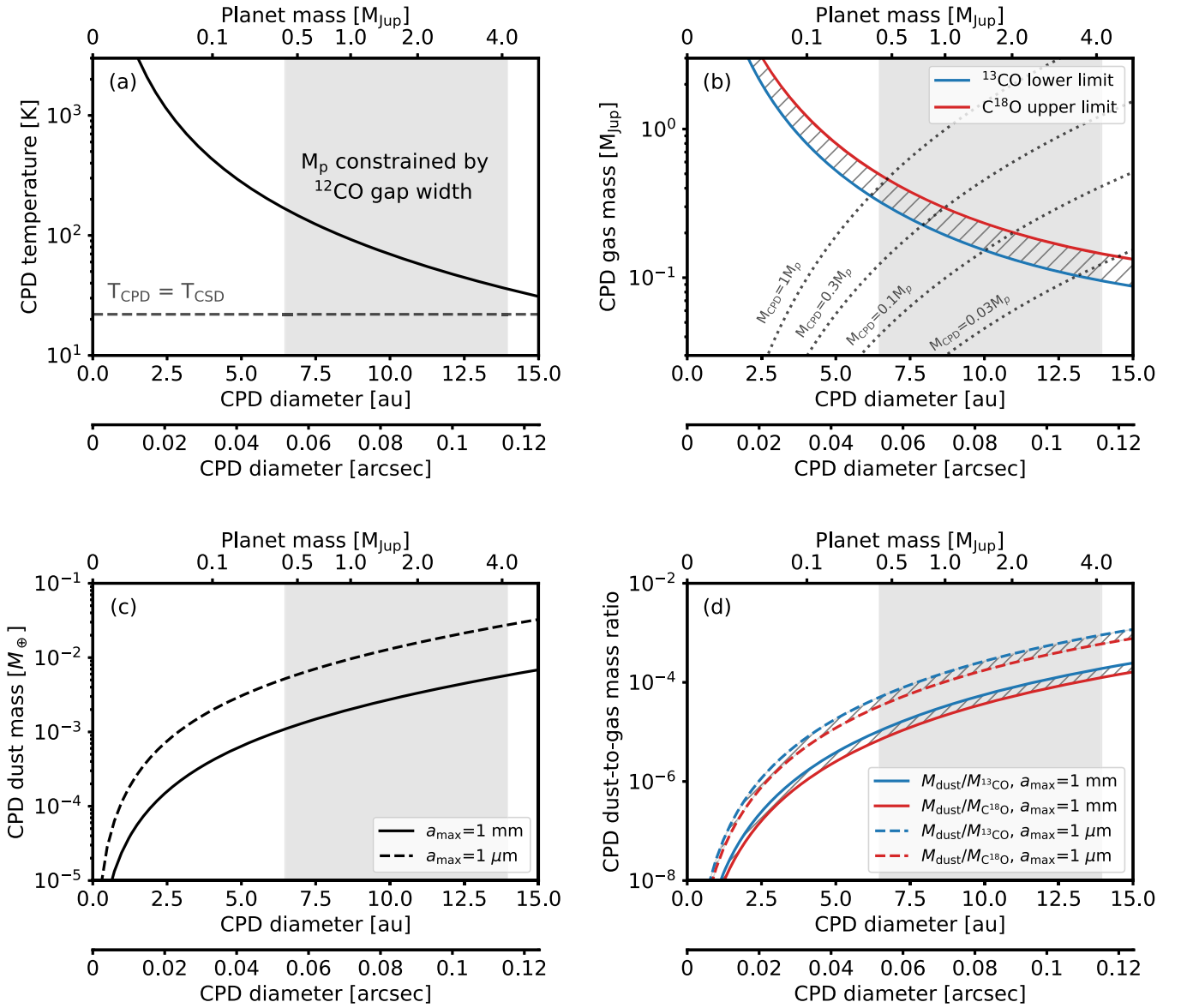
6

Figure 6. (a) The CPD temperature required to explain the observed ^{13}CO emission, as a function of the CPD diameter. The upper horizontal axis shows the planet mass corresponding to the CPD diameter assuming that the CPD radius is 1/3 of the Hill radius: $R_{CPD} = (1/3)R_{Hill} = (1/3)(M_p/3M_*)^{1/3}$. The dashed horizontal line shows AS 209's circumstellar disk temperature at 206 au, 22 K (Law et al. 2021b). The gray-shaded region shows the planet mass constrained by the width of the ^{12}CO gap, 0.42–4.2 M_{Jup}, adopting a range of disk viscosities $\alpha = 10^{-4}$–10^{-2} (see Section 4.1). (b) A lower limit to the CPD gas mass inferred from the ^{13}CO emission (blue) and an upper limit to the CPD gas mass inferred from the null detection of C^{18}O (red). The dashed curves show $M_{CPD} = 1.0, 0.3, 0.1$, and 0.03 M_p (from left to right). (c) The CPD dust mass inferred from the nondetection of the continuum emission. The solid curve assumes a maximum grain size of 1 mm, while the dashed curve assumes a maximum grain size of 1 μm. (d) The CPD dust-to-gas mass ratio obtained from the inferred CPD gas and dust masses. In this figure, the black solid/dashed curves show lower (temperature in panel (a)) or upper (dust mass in panel (c)) limits, while the gray hatched regions present the allowed region in the parameter space bounded by limits from the ^{13}CO (blue) and C^{18}O (red) data.

is the solid angle of the beam. We then calculate the total ^{13}CO number density under the assumption that all energy levels are populated under LTE:

$$n_{^{13}CO,total} = n_{^{13}CO,J} \frac{Z}{2J+1} \exp\left[\frac{hB_e J(J+1)}{kT}\right], \quad (4)$$

where $Z = \sum_{J=0}^{\infty}(2J+1)\exp[-hB_e J(J+1)/kT]$ and $B_e = 55.10101$ GHz is the rotational constant (Müller et al. 2005). We convert the ^{13}CO number density to the total gas mass enclosed in the CPD, adopting the interstellar CO abundance $[^{12}CO]/[H_2] = 10^{-4}$ and ^{13}CO-to-^{12}CO abundance

ratio $[^{13}CO]/[^{12}CO] = 1/60$ (Wilson & Rood 1994). The resulting CPD mass is presented in Figure 6(b). The CPD gas mass is $\simeq 0.095 M_{Jup} (\simeq 30 M_\oplus)$, when $D_{CPD} = 14$ au, and increases with decreasing CPD size because the population in the $J = 2$ level decreases with higher CPD temperature. The CPD-to-planet mass ratio is $M_{CPD}/M_p \gtrsim 0.02$.

In the discussion above, we assumed a CO-to-H$_2$ ratio inferred from the local interstellar medium (ISM). However, near the radial location of the CPD candidate, CO in the AS 209's circumstellar disk is inferred to be depleted in the gas phase by about an order of magnitude compared with the local ISM (Zhang et al. 2021). If the CO in the CPD is depleted at a

comparable level, the CPD-to-planet mass ratio would be $M_{\rm CPD}/M_p \gtrsim 0.2$, a level at which the CPD may be gravitationally unstable.

We can place upper limits on the CPD gas mass from the null detection of $C^{18}O$ emission ($3\sigma \simeq 1.011$ mJy beam^{-1}) following the same approach to ^{13}CO. To do so, we assume that ^{13}CO and $C^{18}O$ share the same line width ($\simeq 400$ m s^{-1}) and temperature (presented in Figure 6(a)). We adopt $A_{21} = 6.01 \times 10^{-7}$ s^{-1} (Schöier et al. 2005), $B_e = 54.89142$ GHz (Müller et al. 2005), and $[C^{18}O]/[^{12}CO] = 1/560$ (Wilson & Rood 1994). The resulting upper limit on the CPD gas mass is presented in Figure 6(b). Interestingly, the null detection of $C^{18}O$ places a tight upper limit that is only about 50% larger than the lower limit obtained with ^{13}CO. When the CPD temperature is larger than the lower limit presented in Figure 6(a), both the ^{13}CO lower limit and $C^{18}O$ upper limit would increase. However, because the rotational constant of the two lines is comparable, the ratio between the upper limit inferred by $C^{18}O$ and the lower limit inferred by ^{13}CO would remain nearly constant (see Equation (4)) and the null detection of $C^{18}O$ would still provide tight constraints.

We can also place constraints on the CPD dust mass from the nondetection of continuum emission ($3\sigma \simeq 26.4$ μJy beam^{-1}). Adopting the DSHARP dust opacity (Birnstiel et al. 2018) with a maximum grain size of 1 mm ($\kappa_\nu = 2.0$ cm^2 g^{-1} at 240 GHz) and the CPD temperature constrained as in Figure 6(a), the CPD dust mass in the optically thin regime is $\lesssim 0.006 M_\oplus \simeq 0.47$ lunar masses. If instead the CPD has only small, micron-sized grains, $\kappa_\nu = 0.42$ cm^2 g^{-1} (Birnstiel et al. 2018) and the CPD dust mass is $\lesssim 0.027 M_\oplus \simeq 2.2$ lunar masses. These results are presented in Figure 6(c).

Using the constraints on the CPD gas and dust mass, we infer the dust-to-gas mass ratio to be $\lesssim 2 \times 10^{-4}$ when the maximum grain size in the CPD is 1 mm and $\lesssim 9 \times 10^{-4}$ when the maximum grain size in the CPD is 1 μm (Figure 6(d)). This suggests that the CPD is likely lacking dust at a level below that in the typical ISM environment, presumably due to a limited dust supply (recall that AS 209's continuum disk is confined within the inner $\simeq 140$ au) and/or the rapid radial drift of dust within the CPD.

4.3. How Did the Planet Form?

Based on the width of the ^{12}CO gap, we infer that the planet's mass is around a Jupiter mass. How did a giant planet form at an orbital radius of 200 au?

One possibility is that the AS 209 disk was gravitationally unstable in the past and the planet formed via gravitational instability (GI; Boss 1997). Limitations of the GI scenario often mentioned in the literature are that the masses of GI-induced fragments are generally large, often in the regime of brown dwarfs, and that GI-induced fragments suffer from tidal disruption and/or rapid radial migration (Baruteau et al. 2011; Zhu et al. 2012). However, recent magnetohydrodynamic simulations including the disk's self-gravity have shown that magnetic fields can limit the mass of the GI-induced fragments to less than a few Jupiter masses, and also can prevent fragments from being tidally disrupted (Deng et al. 2021). It is also shown that orbital migration can stall when the planet actively accretes and carves a deep gap (Fletcher et al. 2019).

Despite recent theoretical developments, one challenge to the GI scenario is that the AS 209 disk has a very small mass of 0.003–0.0045 $M_\odot \simeq 3.1$–$4.7 M_{\rm Jup}$ (Favre et al. 2019;

Zhang et al. 2021). According to the inferred gas surface density profile from Zhang et al. (2021) and the midplane temperature constrained by CO isotopologues from Law et al. (2021b), the Toomre Q parameter (Toomre & Toomre 1972) is >100 at all radii in the AS 209 disk with $Q \simeq 300$ at 200 au, indicating that the disk must be gravitationally stable presently. While it is not impossible that the disk was sufficiently massive in the past, the small present-day disk mass implies that the disk should have lost its mass very efficiently since then.

An alternative to the GI scenario is pebble accretion (Johansen & Lacerda 2010; Ormel & Klahr 2010). In order for the pebble accretion scenario to work, a few things have to be reconciled. First, the continuum emission of the AS 209 disk is confined within the inner $\simeq 140$ au presently. How did the core grow and how did the planet not trap millimeter grains beyond its orbit? We propose that in this scenario, the core of the planet never reached the pebble isolation mass (Morbidelli & Nesvorny 2012) and pebbles could freely drift inward crossing the planet's orbit. Based on scaling relations from hydrodynamic simulations (e.g., Lambrechts et al. 2014; Bitsch et al. 2018), the pebble isolation mass at 200 au in the AS 209 disk ($h/r = 0.118$; Law et al. 2021b) is expected to be $\gtrsim 100 M_\oplus$, much more massive than the critical core mass of $M_{\rm crit} = 10$–$20 M_\oplus$, at which point runaway gas accretion can start (Mizuno 1980). We can thus envision a scenario in which the pebbles that existed beyond the orbit of the core migrated inward, leaving the core behind.

Second, we need to check if sufficient pebbles existed to form a core of the giant planet. To do so, we first estimate the total mass of pebbles necessary to drift toward the core to grow to $10 M_\oplus$ following Lambrechts & Johansen (2014). We obtain $M_{\rm peb} \approx 130 M_\oplus \cdot (M_c/20 M_\oplus)^{1/3} (r/5 \text{ au})^{1/2} ({\rm St}/0.05)^{1/3} \approx 650 M_\oplus$ assuming that the dominant pebble size has a Stokes number of 0.05. The total dust mass in the AS 209 disk is currently about $300 M_\oplus$ (Sierra et al. 2021), but given that it is very unlikely that all the millimeter grains currently inward of the planet's orbit were once beyond 200 au, more efficient pebble accretion than the standard pebble accretion model of Lambrechts & Johansen (2014) is likely required. A few possibilities include the presence of pressure bumps (Pinilla et al. 2012) or a vortex that might have formed early on from the infalling flows from the protostellar envelope (Bae et al. 2015), and changes in sticking properties of grains that lead to the traffic jam effect around snow lines (Drążkowska & Alibert 2017), which can slow down or even halt the radial drift of grains. In fact, it is interesting to note that the midplane gas temperature at the current radial location of the planet ($T \simeq 22$ K; Law et al. 2021b) is close to the expected CO and N_2 freezeout temperature ($T_{\rm frz,CO} = 19$–24 K, $T_{\rm frz,N_2} = 17$–21 K; Huang et al. 2018).

Third, we need to make sure that there had been sufficient time for a core to form via pebble accretion. The timescale for pebble accretion to form a core is given by $t_{\rm PA} \approx 4 \times 10^4$ yr $\cdot (M_{\rm crit}/10 M_\oplus)^{1/3} (r/5 \text{ au})$ (Lambrechts & Johansen 2012). Adopting a critical core mass of $10 M_\oplus$, at 200 au the pebble accretion timescale is $t_{\rm PA} \approx 1.6$ Myr although, as mentioned earlier, slower radial drift or particle trapping can enhance the pebble accretion efficiency and shorten the required time to form the core. Given that the estimated age of AS 209 is 1–2 Myr (Andrews et al. 2009; Öberg et al. 2021), the long core accretion timescale might indicate that the planet could have entered the runaway accretion phase in the last $\lesssim 1$ Myr. If the planet has been accreting $\simeq 1 M_{\rm Jup}$ over the last million years or so, the average

accretion rate would be $\simeq 10^{-6}\,M_{\rm Jup}\,{\rm yr}^{-1}$, orders of magnitude larger than the accretion rate of PDS 70b and c measured from Hα line emission ($10^{-8\pm1}\,M_{\rm Jup}\,{\rm yr}^{-1}$; Wagner et al. 2018; Haffert et al. 2019). Observations of the Hα line can confirm if the planet is indeed undergoing runaway accretion, although long-term monitoring observations are likely required to distinguish steadily high accretion from episodic burst-type accretion (Lubow & Martin 2012).

4.4. Future Observational Direction

We conclude the discussion by listing a few future directions from the observational perspective. While we could only place upper/lower limits from the existing data, future higher-level transition observations of ^{13}CO (together with the existing ^{13}CO $J = 2 - 1$ data) will allow us to determine whether ^{13}CO is optically thick or thin, and thus place stronger constraints on the CPD temperature. As shown in Figure 6(b), the null detection of C^{18}O already placed a tight upper limit on the CPD gas mass that is only about 50% larger than the lower limit inferred by ^{13}CO. Deeper C^{18}O observations (by a factor of $\simeq 2$ in sensitivity assuming that isotope-selective photodissociation is not important) should thus detect the CPD and place stringent constraints on the CPD gas mass. The existing data are limited by a $200\,{\rm m\,s}^{-1}$ velocity resolution and we presently cannot conclude whether the point-source emission is consistent with a rotationally supported disk or a pressure-supported envelope that is potentially heated by an embedded planet (e.g., Alves et al. 2020). Future observations with higher velocity resolution will enable us to distinguish the two scenarios and to dynamically constrain the planet mass from the rotation of the CPD. High-spatial/velocity-resolution observations will also enable us to constrain the geometry of the CPD (e.g., position angle, inclination) from the disk rotation. Knowing the CPD geometry will allow us to place more accurate constraints on the CPD temperature and mass. In addition, estimating the obliquity of the CPD can help us to better understand the formation mechanism and environment of the CPD-hosting planet, in particular, whether the planet had formed in a turbulent environment that would induce large obliquities (see, e.g., Bryan et al. 2020; Jennings & Chiang 2021). The inferred CPD temperature suggests that heating sources localized to the CPD must be present. Such planetary/CPD heating can produce chemical asymmetries in the circumstellar disk, which are shown to be detectable with high-sensitivity molecular-line observations using ALMA (Cleeves et al. 2015). Besides additional ALMA observations, future observations in the infrared wavelengths using the James Webb Space Telescope and ground-based telescopes would independently confirm the planet/CPD and allow us to probe the thermal emission from the planet, which can help to constrain the mass of the planet. In addition, searching for accretion signatures (e.g., Hα line emission) would yield invaluable constraints on the current position of the planet in its evolutionary stages.

5. Conclusion

We report the discovery of a CPD candidate in ^{13}CO $J = 2 - 1$ emission, embedded in the AS 209 disk at a radial distance of about 200 au. This is the first instance of CPD detection via gaseous emission, allowing us to probe the overall CPD mass. The CPD candidate is located in the middle of an annular gap

identified in ^{12}CO and near-infrared scattered-light observations and is associated with localized velocity perturbations in ^{12}CO (see Figure 5). The coincidence of these features strongly suggests that we are witnessing the signature of a giant planet and its CPD embedded in the AS 209 disk.

The CPD is spatially unresolved with a 117×82 mas beam, indicating that its diameter is $\lesssim 14$ au. Based on the ^{13}CO intensity, we were able to constrain the CPD temperature and gas mass. The CPD temperature is $\gtrsim 35$ K, greater than the circumstellar disk temperature at the midplane of the radial location of the CPD, 22 K (Law et al. 2021b). This suggests that there must be heating sources localized to the CPD in order to maintain the high temperature. Potential sources include the planet's thermal/accretion heating, the CPD's internal viscous/turbulent heating, and shock/compressional heating by infalling circumstellar disk material. The CPD gas mass is $\gtrsim 0.095\,M_{\rm Jup} \simeq 30\,M_{\oplus}$, adopting a standard ^{13}CO abundance. Based on the nondetection of continuum emission toward the CPD location, we found that the CPD has $\lesssim 0.027\,M_{\oplus} \simeq 2.2$ lunar masses of dust. Together with the inferred gas mass, this indicates a low dust-to-gas mass ratio of $\lesssim 9 \times 10^{-4}$ within the CPD, presumably due to a limited dust supply to the CPD and/or rapid radial drift of dust within the CPD.

The estimated age of the system is only 1–2 Myr (Andrews et al. 2009; Öberg et al. 2021). If confirmed, this CPD-hosting planet would be one of the youngest exoplanets detected to date. Observing planets at this young age allows us to place strong constraints on the mechanism and timescale of planet formation, crucial to gaining new insights into the formation and evolution of giant planets.

Appendix A
Additional Channel Maps

Figure 7 presents the ^{12}CO channel maps for the image cube with a half-channel velocity shift. Figures 8 and 9 present the ^{13}CO channel maps for the fiducial image cube and the cube with a half-channel velocity shift.
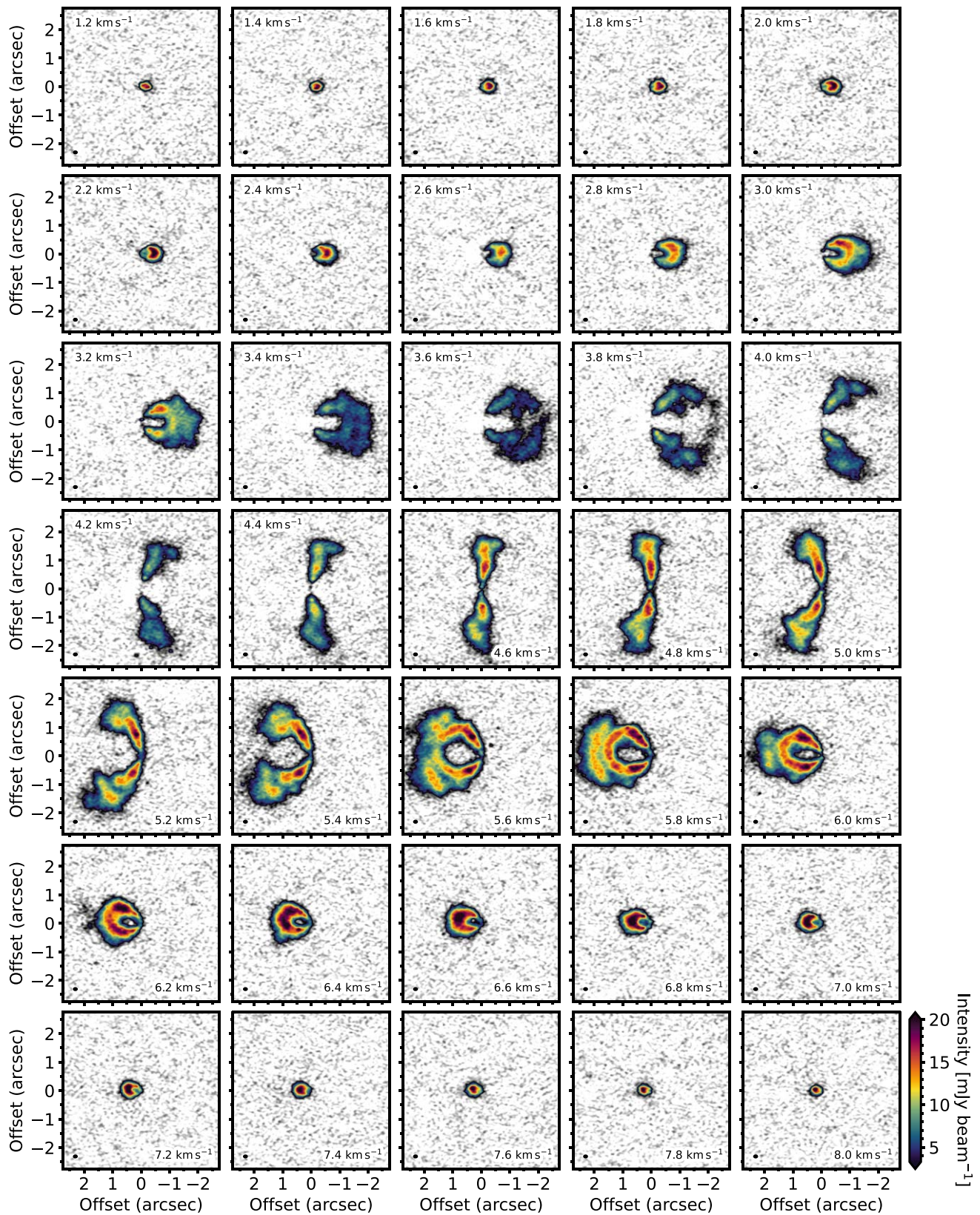
Figure 7. Channel maps showing the ^{12}CO $J = 2-1$ emission from the half-channel-shifted image cube. The color map starts at 5σ. The synthesized beam is shown in the lower-left corner of each panel. An interactive version of the figure made with TRIVIA is available. Controls at the top allow the user to zoom, pan, and rescale the images. The controls at the bottom include a slider and play/stop buttons to cycle through the channel maps. Placing the cursor in the image will display the positional offset and intensity.

Figure 8. Channel maps showing the ^{13}CO $J = 2 - 1$ emission. The color map starts at 5σ. The synthesized beam is shown in the lower-left corner of each panel. An interactive version of the figure made with TRIVIA is available. Controls at the top allow the user to zoom, pan, and rescale the images. The controls at the bottom include a slider and play/stop buttons to cycle through the channel maps. Placing the cursor in the image will display the positional offset and intensity.
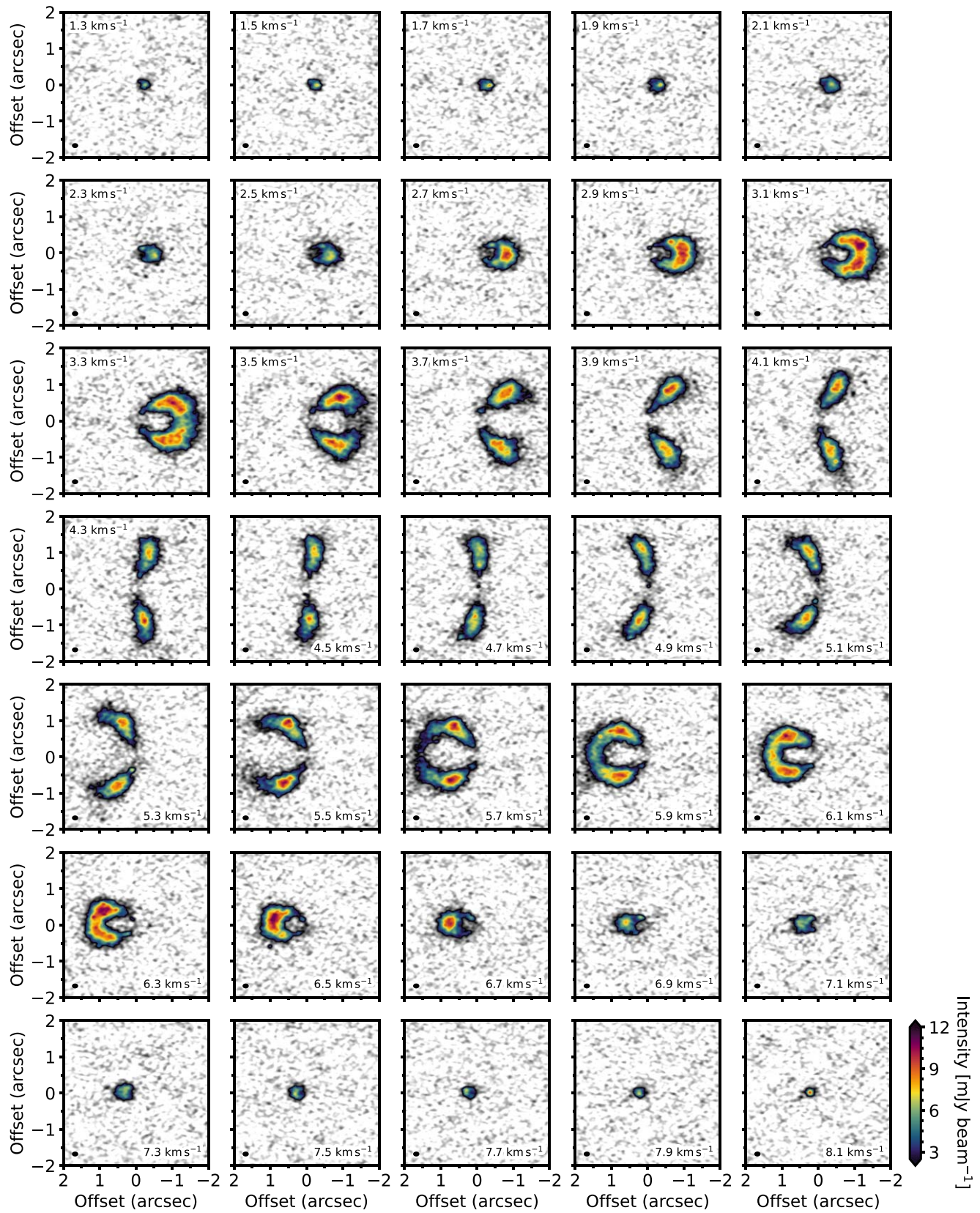
Figure 9. Same as Figure 8, but for the half-channel-shifted image cube. An interactive version of the figure made with `TRIVIA` is available. Controls at the top allow the user to zoom, pan, and rescale the images. The controls at the bottom include a slider and play/stop buttons to cycle through the channel maps. Placing the cursor in the image will display the positional offset and intensity.
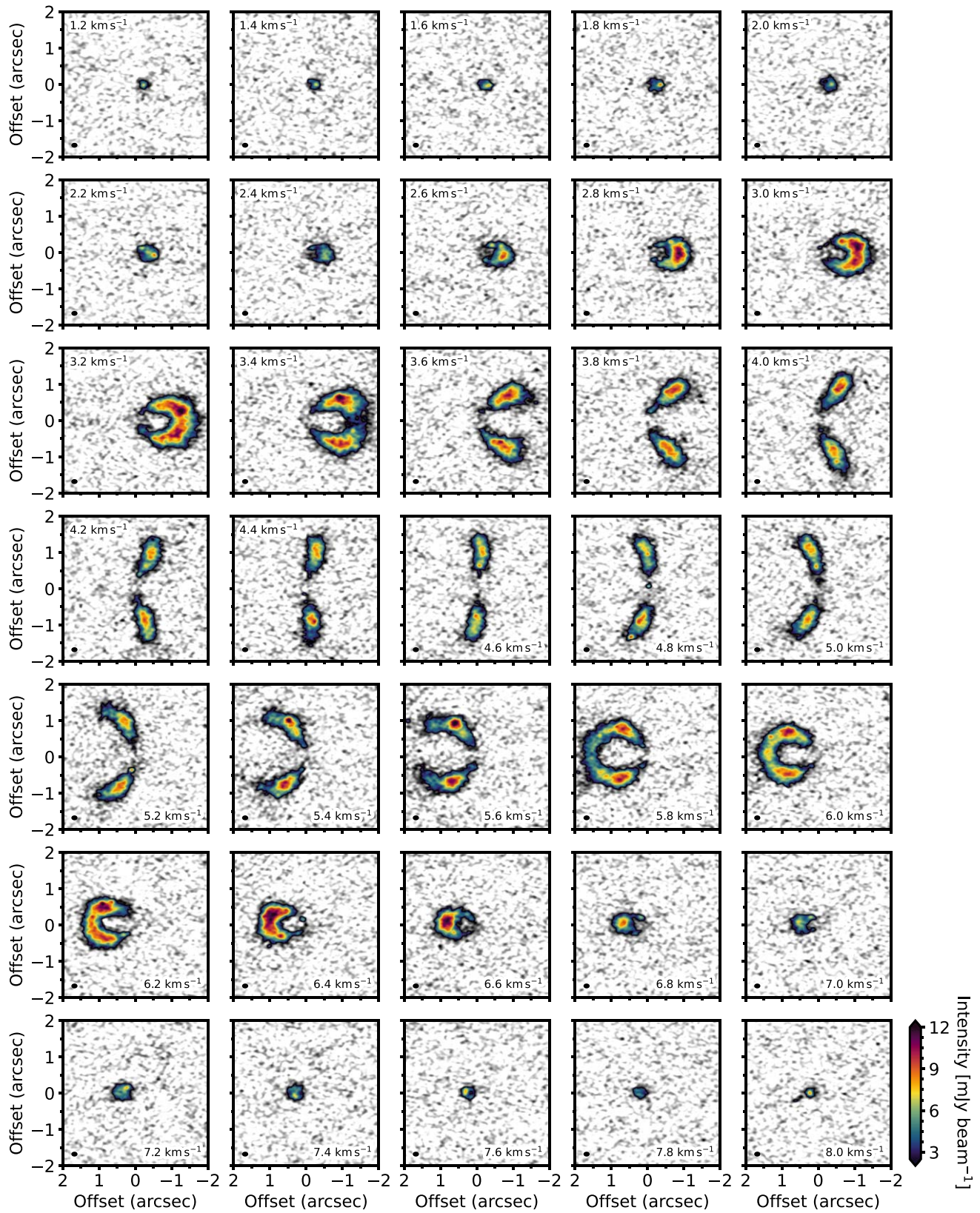
Appendix B
^{13}CO Emission with Various Imaging Parameters

Tables 1 and 2 present a summary of the ^{13}CO point source in the images adopting various `robust` parameters from −1 to 2. The rms noise is measured within the synthesized beam

around the CPD over the first 20 line-free channels of the cube ($v_{\rm LSR} = 14.7$–$10.9\,{\rm km\,s^{-1}}$). The central velocity, FWHM, peak intensity, and integrated intensity are obtained from Gaussian fitting of the emission within the synthesized beam around the CPD, using the CASA task `specfit`.

Table 1
Summary of CPD Properties in Various JvM-corrected Images

Briggs Parameter	Beam (mas × mas)	PA (deg)	rms Noise (mJy beam^{-1})	Central Velocity (km s^{-1})	FWHM (km s^{-1})	Peak Intensity (mJy beam^{-1})	Integrated Intensity (mJy beam^{-1} km s^{-1})
−1	118 × 83	−84.561	1.184	4.813 ± 0.031	0.388 ± 0.079	5.41 ± 0.92	2.23 ± 0.59
−0.75	118 × 83	−84.943	1.098	4.809 ± 0.029	0.384 ± 0.075	5.52 ± 0.90	2.26 ± 0.57
−0.5	119 × 84	−85.306	1.015	4.813 ± 0.027	0.381 ± 0.071	5.71 ± 0.88	2.32 ± 0.56
−0.25	120 × 85	−85.660	0.950	4.815 ± 0.026	0.385 ± 0.067	5.77 ± 0.84	2.36 ± 0.54
0	123 × 88	−86.495	0.788	4.810 ± 0.021	0.381 ± 0.056	5.90 ± 0.71	2.39 ± 0.45
0.25	130 × 94	−87.737	0.624	4.812 ± 0.017	0.393 ± 0.043	5.75 ± 0.52	2.40 ± 0.34
0.5	140 × 104	−89.062	0.457	4.812 ± 0.012	0.404 ± 0.029	5.65 ± 0.35	2.43 ± 0.23
0.75	155 × 118	+89.836	0.327	4.815 ± 0.080	0.418 ± 0.020	6.04 ± 0.24	2.69 ± 0.16
1	172 × 133	−89.898	0.243	4.819 ± 0.061	0.439 ± 0.015	6.56 ± 0.19	3.07 ± 0.14
1.25	187 × 146	−88.779	0.208	4.824 ± 0.005	0.447 ± 0.012	7.09 ± 0.17	3.37 ± 0.12
1.5	195 × 154	−88.138	0.195	4.827 ± 0.005	0.453 ± 0.012	7.60 ± 0.17	3.67 ± 0.12
1.75	198 × 157	−86.890	0.191	4.823 ± 0.005	0.455 ± 0.011	7.79 ± 0.17	3.77 ± 0.12
2	200 × 158	−86.819	0.190	4.828 ± 0.005	0.453 ± 0.011	7.89 ± 0.17	3.80 ± 0.13

Table 2
Summary of CPD Properties in Various JvM-corrected Images with a Half-channel Velocity Shift

| Briggs Parameter	Beam (mas×mas)	PA (deg)	rms Noise (mJy beam^{-1})	Central Velocity (km s^{-1})	FWHM (km s^{-1})	Peak Intensity (mJy beam^{-1})	Integrated Intensity (mJy beam^{-1} km s^{-1})
−1	117 × 82	−85.632	1.268	4.806 ± 0.026	0.301 ± 0.042	7.70 ± 1.00	2.45 ± 0.47
−0.75	117 × 83	−85.692	1.256	4.806 ± 0.025	0.293 ± 0.039	8.00 ± 1.00	2.50 ± 0.46
−0.5	118 × 83	−85.828	1.221	4.807 ± 0.024	0.294 ± 0.038	8.05 ± 0.98	2.52 ± 0.45
−0.25	119 × 84	−86.245	1.105	4.808 ± 0.022	0.286 ± 0.033	8.33 ± 0.90	2.54 ± 0.40
0	122 × 87	−86.972	0.977	4.809 ± 0.019	0.281 ± 0.028	8.64 ± 0.80	2.59 ± 0.35
0.25	128 × 93	−88.135	0.727	4.815 ± 0.014	0.284 ± 0.022	8.32 ± 0.59	2.52 ± 0.27
0.5	138 × 103	−89.390	0.543	4.819 ± 0.010	0.292 ± 0.017	8.03 ± 0.42	2.50 ± 0.20
0.75	153 × 116	+89.917	0.370	4.825 ± 0.006	0.300 ± 0.011	8.32 ± 0.29	2.66 ± 0.14
1	170 × 132	−89.857	0.272	4.828 ± 0.005	0.319 ± 0.009	9.00 ± 0.23	3.05 ± 0.12
1.25	185 × 144	−89.430	0.233	4.834 ± 0.004	0.335 ± 0.008	9.54 ± 0.21	3.40 ± 0.11
1.5	195 × 153	−87.999	0.218	4.836 ± 0.004	0.346 ± 0.008	9.85 ± 0.21	3.62 ± 0.12
1.75	198 × 157	−86.536	0.213	4.834 ± 0.004	0.344 ± 0.008	10.31 ± 0.21	3.78 ± 0.11
2	200 × 157	−87.365	0.212	4.836 ± 0.004	0.345 ± 0.008	10.45 ± 0.21	3.84 ± 0.12
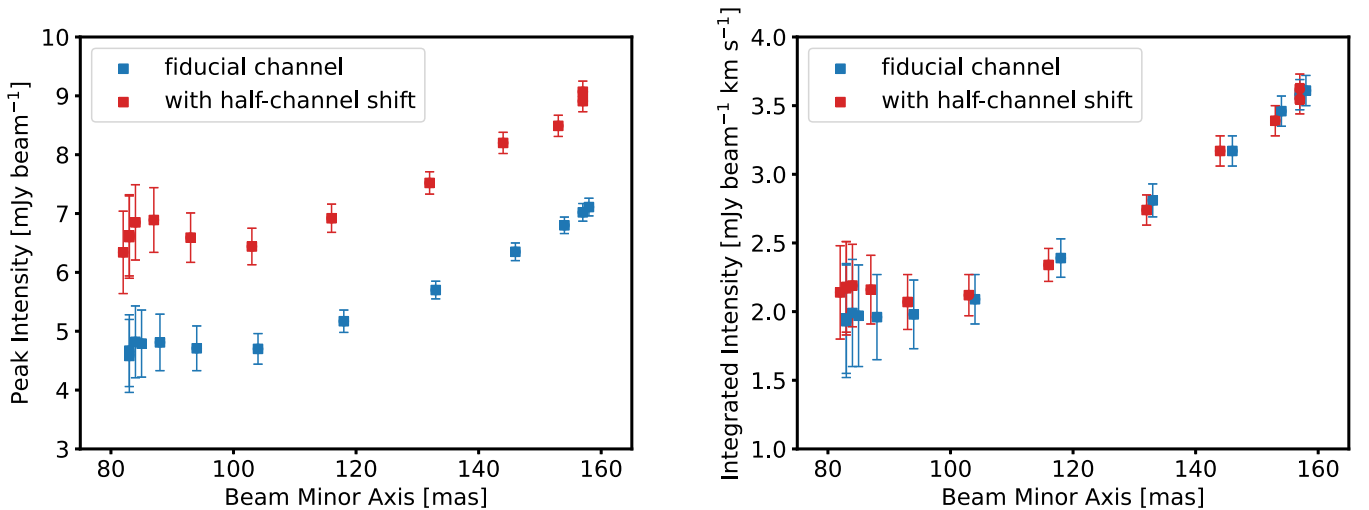
Figure 10. (Left) Peak intensity as a function of the beam minor axis. (Right) Integrated intensity as a function of the beam minor axis. Note that both peak intensity and integrated intensity stay constant when the beam is ≲120 mas, suggesting that the CPD is spatially unresolved. When the beam is >120 mas, the peak intensity and integrated intensity increase due to the contamination from the circumstellar disk. In both panels, blue points present intensities in the fiducial image cube whereas red points present intensities in the image cube where the half-channel shift is applied.

In Figure 10, we present the peak and integrated intensities as a function of the beam minor axis. The peak and integrated intensities remain constant within uncertainties when the beam minor axis is $\lesssim 120$ mas, indicating that the point source is spatially unresolved at those scales. The peak and integrated intensities increase for larger beam sizes because the beam contains emission from the AS 209 disk.

Appendix C
Analysis with JvM-uncorrected Images

Figure 11 presents ^{13}CO channel maps without JvM correction. Note that the CPD is clearly seen in all three

channels even before the JvM correction is applied, with the peak intensity of 8.80, 13.5, and 8.47 mJy beam^{-1}, respectively. The peak intensity-to-noise ratio is about 6, 9, and 6 in the three channels, indicating that the detection is statistically significant in the JvM-uncorrected image.

In Figure 12, we present the radial integrated intensity profiles. At $1\rlap{.}''7$, the integrated intensity of the point source is 4.37 mJy beam^{-1} km s^{-1}, while the integrated intensity excluding the point source is 2.02 mJy beam^{-1} km s^{-1} with a standard deviation of $\sigma = 0.77$ mJy beam^{-1} km s^{-1}. After subtracting the contribution from the gap, the point source is detected at a 4.4σ significance.
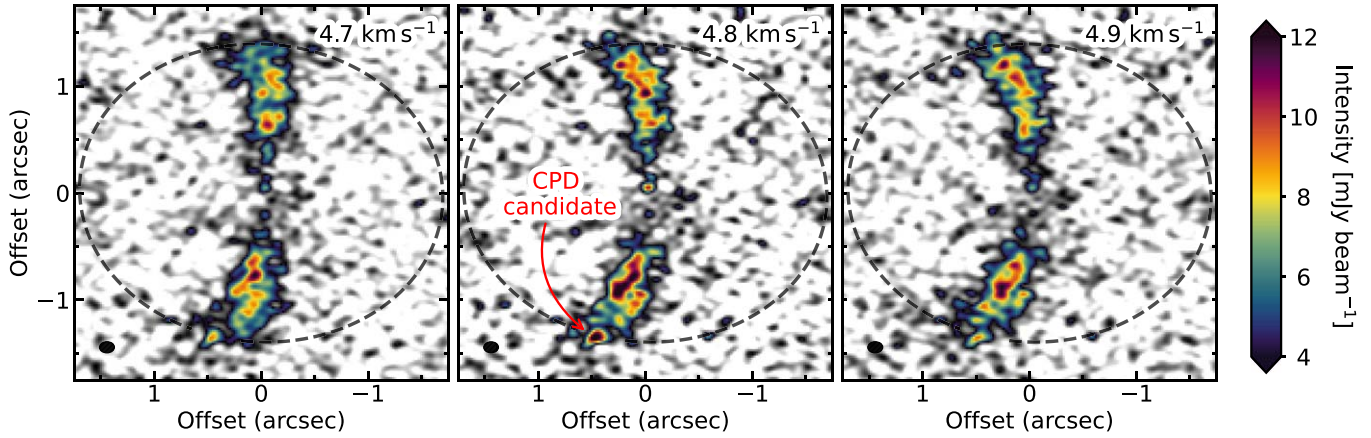

Figure 11. Same as Figure 2, but without the JvM correction. Note that the CPD is clearly seen in the JvM-uncorrected image.
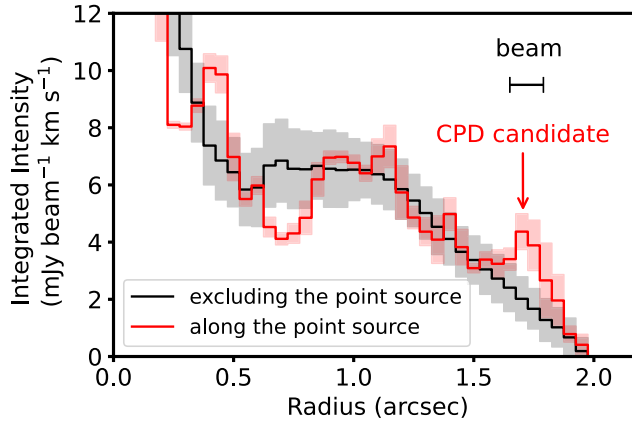

Figure 12. Same as Figure 3, but the radial integrated intensity profiles are derived using the JvM-uncorrected image.

ORCID iDs

Jaehan Bae ⓘ https://orcid.org/0000-0001-7258-770X
Richard Teague ⓘ https://orcid.org/0000-0003-1534-5186
Sean M. Andrews ⓘ https://orcid.org/0000-0003-2253-2270
Myriam Benisty ⓘ https://orcid.org/0000-0002-7695-7605
Stefano Facchini ⓘ https://orcid.org/0000-0003-4689-2684
Maria Galloway-Sprietsma ⓘ https://orcid.org/0000-0002-5503-5476
Ryan A. Loomis ⓘ https://orcid.org/0000-0002-8932-1219
Yuri Aikawa ⓘ https://orcid.org/0000-0003-3283-6884
Felipe Alarcón ⓘ https://orcid.org/0000-0002-2692-7862
Edwin Bergin ⓘ https://orcid.org/0000-0003-4179-6394
Jennifer B. Bergner ⓘ https://orcid.org/0000-0002-8716-0482
Alice S. Booth ⓘ https://orcid.org/0000-0003-2014-2121
Gianni Cataldi ⓘ https://orcid.org/0000-0002-2700-9676
L. Ilsedore Cleeves ⓘ https://orcid.org/0000-0003-2076-8001
Ian Czekala ⓘ https://orcid.org/0000-0002-1483-8811
Viviana V. Guzmán ⓘ https://orcid.org/0000-0003-4784-3040
Jane Huang ⓘ https://orcid.org/0000-0001-6947-6072
John D. Ilee ⓘ https://orcid.org/0000-0003-1008-1142
Nicolas T. Kurtovic ⓘ https://orcid.org/0000-0002-2358-4796
Charles J. Law ⓘ https://orcid.org/0000-0003-1413-1776
Romane Le Gal ⓘ https://orcid.org/0000-0003-1837-3772
Yao Liu ⓘ https://orcid.org/0000-0002-7616-666X
Feng Long ⓘ https://orcid.org/0000-0002-7607-719X
François Ménard ⓘ https://orcid.org/0000-0002-1637-7393
Karin I. Öberg ⓘ https://orcid.org/0000-0001-8798-1347
Laura M. Pérez ⓘ https://orcid.org/0000-0002-1199-9564
Chunhua Qi ⓘ https://orcid.org/0000-0001-8642-1786
Kamber R. Schwarz ⓘ https://orcid.org/0000-0002-6429-9457
Anibal Sierra ⓘ https://orcid.org/0000-0002-5991-8073
Catherine Walsh ⓘ https://orcid.org/0000-0001-6078-786X
David J. Wilner ⓘ https://orcid.org/0000-0003-1526-7587
Ke Zhang ⓘ https://orcid.org/0000-0002-0661-7517

References

Alves, F. O., Cleeves, L. I., Girart, J. M., et al. 2020, ApJL, 904, L6
Andrews, S. M., Elder, W., Zhang, S., et al. 2021, ApJ, 916, 51
Andrews, S. M., Huang, J., Pérez, L. M., et al. 2018, ApJL, 869, L41
Andrews, S. M., Wilner, D. J., Hughes, A. M., Qi, C., & Dullemond, C. P. 2009, ApJ, 700, 1502
Avenhaus, H., Quanz, S. P., Garufi, A., et al. 2018, ApJ, 863, 44
Bae, J. 2022, TRIVIA: Tools foR Interactive fits VIsuAlization, v1.0.0, Zenodo, doi:10.5281/zenodo.6786391
Bae, J., Hartmann, L., & Zhu, Z. 2015, ApJ, 805, 15
Baruteau, C., Meru, F., & Paardekooper, S.-J. 2011, MNRAS, 416, 1971
Benisty, M., Bae, J., Facchini, S., et al. 2021, ApJL, 916, L2
Birnstiel, T., Dullemond, C. P., Zhu, Z., et al. 2018, ApJL, 869, L45
Bitsch, B., Morbidelli, A., Johansen, A., et al. 2018, A&A, 612, A30
Boss, A. P. 1997, Sci, 276, 1836
Bryan, M. L., Chiang, E., Bowler, B. P., et al. 2020, AJ, 159, 181
Bryan, M. L., Chiang, E., Morley, C. V., Mace, G. N., & Bowler, B. P. 2021, AJ, 162, 217
Casassus, S., & Carcamo, M. 2022, MNRAS, 513, 5790
Casassus, S., & Pérez, S. 2019, ApJL, 883, L41
Cleeves, L. I., Bergin, E. A., & Harries, T. J. 2015, ApJ, 807, 2
Czekala, I., Loomis, R. A., Teague, R., et al. 2021, ApJS, 257, 2

Deng, H., Mayer, L., & Helled, R. 2021, NatAs, 5, 440
Drążkowska, J., & Alibert, Y. 2017, A&A, 608, A92
Favre, C., Fedele, D., Maud, L., et al. 2019, ApJ, 871, 107
Fedele, D., Tazzari, M., Booth, R., et al. 2018, A&A, 610, A24
Fletcher, M., Nayakshin, S., Stamatellos, D., et al. 2019, MNRAS, 486, 4398
Fung, J., Zhu, Z., & Chiang, E. 2019, ApJ, 887, 152
Gaia Collaboration, Brown, A. G. A., Vallenari, A., et al. 2021, A&A, 649, A1
Guzmán, V. V., Huang, J., Andrews, S. M., et al. 2018, ApJL, 869, L48
Haffert, S. Y., Bohn, A. J., de Boer, J., et al. 2019, NatAs, 3, 749
Huang, J., Andrews, S. M., Dullemond, C. P., et al. 2018, ApJL, 869, L42
Huang, J., Öberg, K. I., & Andrews, S. M. 2016, ApJL, 823, L18
Hunter, J. D. 2007, CSE, 9, 90
Isella, A., Benisty, M., Teague, R., et al. 2019, ApJL, 879, L25
Isella, A., Chandler, C. J., Carpenter, J. M., Pérez, L. M., & Ricci, L. 2014, ApJ, 788, 129
Jennings, R. M., & Chiang, E. 2021, MNRAS, 507, 5187
Johansen, A., & Lacerda, P. 2010, MNRAS, 404, 475
Jorsater, S., & van Moorsel, G. A. 1995, AJ, 110, 2037
Kanagawa, K. D., Muto, T., Tanaka, H., et al. 2016, PASJ, 68, 43
Korycansky, D. G., Bodenheimer, P., & Pollack, J. B. 1991, Icar, 92, 234
Lambrechts, M., & Johansen, A. 2012, A&A, 544, A32
Lambrechts, M., & Johansen, A. 2014, A&A, 572, A107
Lambrechts, M., Johansen, A., & Morbidelli, A. 2014, A&A, 572, A35
Law, C. J., Loomis, R. A., Teague, R., et al. 2021a, ApJS, 257, 3
Law, C. J., Teague, R., Loomis, R. A., et al. 2021b, ApJS, 257, 4
Lin, D. N. C., & Papaloizou, J. 1986, ApJ, 309, 846
Lubow, S. H., & Martin, R. G. 2012, ApJL, 749, L37
Lubow, S. H., Seibert, M., & Artymowicz, P. 1999, ApJ, 526, 1001
McMullin, J. P., Waters, B., Schiebel, D., Young, W., & Golap, K. 2007, in ASP Conf. Ser., 376, Astronomical Data Analysis Software and Systems XVI, ed. R. A. Shaw, F. Hill, & D. J. Bell (San Francisco, CA: ASP), 127
Mizuno, H. 1980, PThPh, 64, 544
Morbidelli, A., & Nesvorny, D. 2012, A&A, 546, A18
Müller, H. S., Schlöder, F., Stutzki, J., & Winnewisser, G. 2005, JMoSt, 742, 215
Öberg, K. I., Guzmán, V. V., Walsh, C., et al. 2021, ApJS, 257, 1
Ormel, C. W., & Klahr, H. H. 2010, A&A, 520, A43
Paardekooper, S.-J., Dong, R., Duffell, P., et al. 2022, arXiv:2203.09595
Perez, S., Dunhill, A., Casassus, S., et al. 2015, ApJL, 811, L5
Pérez, S., Marino, S., Casassus, S., et al. 2019, MNRAS, 488, 1005
Pineda, J. E., Szulágyi, J., Quanz, S. P., et al. 2019, ApJ, 871, 48
Pinilla, P., Benisty, M., & Birnstiel, T. 2012, A&A, 545, A81
Pinte, C., Price, D. J., Ménard, F., et al. 2018, ApJL, 860, L13
Pinte, C., Teague, R., Flaherty, K., et al. 2022, arXiv:2203.09528
Pinte, C., van der Plas, G., Ménard, F., et al. 2019, NatAs, 3, 1109
Schöier, F. L., van der Tak, F. F. S., van Dishoeck, E. F., & Black, J. H. 2005, A&A, 432, 369
Sierra, A., Pérez, L. M., Zhang, K., et al. 2021, ApJS, 257, 14
Szulágyi, J., Masset, F., Lega, E., et al. 2016, MNRAS, 460, 2853
Szulágyi, J., & Mordasini, C. 2017, MNRAS, 465, L64
Teague, R. 2019, JOSS, 4, 1632
Teague, R., Bae, J., & Bergin, E. A. 2019a, Natur, 574, 378
Teague, R., Bae, J., Birnstiel, T., & Bergin, E. A. 2018, ApJ, 868, 113
Teague, R., Bae, J., Huang, J., & Bergin, E. A. 2019b, ApJL, 884, L56
Teague, R., & Foreman-Mackey, D. 2018, Bettermoments: A Robust Method To Measure Line Centroids, vv1.0, Zenodo, doi:10.5281/zenodo.1419754
Toomre, A., & Toomre, J. 1972, ApJ, 178, 623
van der Walt, S., Colbert, S. C., & Varoquaux, G. 2011, CSE, 13, 22
Wagner, K., Follete, K. B., Close, L. M., et al. 2018, ApJL, 863, L8
Ward, W. R., & Canup, R. M. 2010, AJ, 140, 1168
Wilson, T. L., & Rood, R. 1994, ARA&A, 32, 191
Wu, Y.-L., Bowler, B. P., Sheehan, P. D., et al. 2022, ApJL, 930, L3
Yu, H., Teague, R., Bae, J., & Öberg, K. 2021, ApJL, 920, L33
Yun, H., Kim, W.-T., Bae, J., & Han, C. 2019, ApJ, 884, 142
Zhang, K., Booth, A. S., Law, C. J., et al. 2021, ApJS, 257, 5
Zhang, S., Zhu, Z., Huang, J., et al. 2018, ApJL, 869, L47
Zhu, Z., Hartmann, L., Nelson, R. P., & Gammie, C. F. 2012, ApJ, 746, 110